

Machine Learning Based Mesh Movement for Non-Hydrostatic Tsunami Simulation

Yezhang Li, Stephan C. Kramer, Matthew D. Piggott

*Department of Earth Science and Engineering, Imperial College London, South
Kensington Campus, London, SW7 2AZ, United Kingdom*

Abstract

This study investigates the use of machine learning based mesh adaptivity, specifically mesh movement methods (UM2N), with depth integrated non-hydrostatic shallow water models. Motivation for this comes from the need for models which balance efficiency and accuracy for use in probabilistic coastal hazard assessment. Implementations are built on the discontinuous Galerkin finite-element (DG-FE) based software, Thetis, which leverages the partial differential equation (PDE) framework Firedrake for automated code generation. Verification on benchmark test cases and validation against laboratory measurements of coastal hazards, focusing on tsunami propagation, run-up, and inundation is performed. In these tests, the UM2N-driven meshes help resolve key non-hydrostatic dynamics and yield numerical solutions in close agreement with reference computations and measured data. Numerical results indicate that the UM2N surrogate based approach significantly accelerates conventional mesh movement techniques and has high robustness over long integration periods and under strongly nonlinear wave conditions.

Keywords:

Shallow Water Equations; Non-Hydrostatic; Discontinuous Galerkin; Finite Element Method, Mesh Movement; Monge–Ampère; Deep Learning; Neural Network

1. Introduction

Accurate modeling of coastal tsunami has been a challenging research topic for many decades, with a goal of effective hazard assessments in the

1
2
3

face of complex coastal topography, changeable multi-scale flow dynamics and the impacts of flooding and drying processes. Unlike hydrostatic models that are commonly used for large-scale tsunami simulations, it is necessary to consider non-hydrostatic effects in coastal tsunami scenarios in order to represent with sufficient accuracy complex nearshore wave processes, especially for both short waves and relatively long waves with high non-linearity. According to Pan et al. (2019), the propagation of strong dispersive or non-linear waves towards the shore may undergo significant wave steepening and transformation due to variations in water depth or bottom friction. The associated shoaling and funnelling primarily arise from the combined effects of frequency dispersion caused by non-hydrostatic impacts and wave-wave or wave-structure interactions from non-linearity (Cui et al., 2012; Pan et al., 2019). However, it is difficult to represent these phenomena in non-linear shallow water equation (NSWE) models under hydrostatic assumptions. Hence, it is important to consider non-hydrostatic effects in coastal tsunami simulation. A number of non-hydrostatic coastal ocean models have been developed via adopting the approach introduced by Zijlema and Stelling (2005). In addition, several Boussinesq wave models have been developed to enhance their applicability in capturing wave diffraction and refraction for coastal wave propagation (See Wei and Kirby (1995), Liang et al. (2013) and Shi et al. (2013)). This is because the original Boussinesq-type equations take weak dispersion into consideration.

However, the increased accuracy of non-hydrostatic modeling comes with a substantial computational cost, impacting on feasible mesh resolutions, simulation time scales and domain sizes, and the number of simulations that can be conducted. Scientists and engineers in computational fluid dynamics have always sought a balance between accuracy and computational costs in their models. In coastal ocean modelling, a series of simplified non-hydrostatic models have been developed to reduce computational costs, instead of solving the full 3D Navier-Stokes (N-S) equations. According to Pan et al. (2019) and Stansby and Zhou (1998), one of the popular simplified approaches is a type of non-hydrostatic model that decomposes the total pressure into a hydrostatic part and a non-hydrostatic part, in which the non-hydrostatic pressure term is retained in the hydrostatic equations to capture the effect of vertical flow acceleration. In Thetis, there are also DG-FE based non-hydrostatic modelling approaches via both multi-layer and depth-integrated systems developed by Pan et al. (2019) based upon the pioneering work of DG-FE based approaches (following Kärnä et al. (2018)) and

layer-integrated non-hydrostatic models (see Zijlema and Stelling (2005), Wei and Jia (2013) and Cui et al. (2012)) for coastal ocean problems. While such non-hydrostatic approaches still have limitations in capturing wave breaking/overtopping, their favourable properties can be quite significant for large-scale applications in coastal ocean/tsunami simulation.

On the other hand, although significant progress has been made in the development of non-hydrostatic models for coastal ocean simulations, most of them rely on fixed and quasi-uniform meshes such as SWASH (Zijlema et al., 2011) and NHWAVE (Ma et al., 2012). The main limitation of structured/uniform meshes is the relatively poor representation of the complex coastline and coastal topography, and inflexibility to focus resolution and dynamically adapt on time-varying changes in the fluid dynamics, especially when tracking wave propagation (usually tsunami) across the ocean (Piggott et al., 2005; Davis and LeVeque, 2016). An alternative way to resolve this problem is to adopt mesh adaptation methods, which allows for mesh resolution to be optimised in order to maximise accuracy while minimising computational costs, and allowing for large geographical scale simulations to be conducted at the same time as representing detailed coastal processes. In general, there are two main types of mesh adaptation methods: h-adaptation and r-adaptation. Broadly speaking, classical h-adaptive methods refine the mesh resolution by locally adding or removing mesh nodes, which changes the local topological structure. While r-adaptive methods change mesh resolution by moving the locations of mesh nodes but fixing the total number of nodes and their connectivity. In the past decade, according to Wallwork (2021), the use of optimal transport mesh movement driven by the solutions of Monge–Ampère (MA) type equations, related to r-adaptivity, has been advocated in the simulation of geophysical flows by Budd and Williams (2009) and McRae et al. (2018), etc. This enables mesh movement methods based on the MA equations which can also be applied in solving tsunami propagation problems based on NSWE. In the Thetis framework, Clare et al. (2021) applied MA-based mesh movement in NSWE based hydro-morphodynamic problems such as “Migrating Trench” and wet-dry interface test cases. Although optimal transport based MA mesh movement has significant performance advantages in preventing mesh tangling issues, such robust mesh movement methods lead to a significant increase in computational costs (Clare et al., 2021; Song et al., 2024).

With the recent explosion in the development of AI techniques in PDE solvers, there has been increasing interest in AI-based mesh adaptation ap-

proaches. According to Song et al. (2024), a series of these methods focusing on mesh generation and mesh refinement have been developed (follow the work of Fidkowski and Chen (2021), Huang et al. (2021), Yang et al. (2023) and Zhang et al. (2020)), which provide a number of new opportunities and possibilities to address the limitations of traditional mesh adaptation approaches, including high computational costs. To alleviate the mesh tangling and enhance the flexibility of mesh adaptation for traditional MA-based mesh movement, Song et al. (2024) introduced a novel learning-based approach called Mesh Movement Network (M2N) that consists of a Neural Spline model or a Graph Attention Network (GAT). It presented a more direct way to generate the adapted meshes via a neural network compared with the previous AI-based mesh adaptation. As an enhancement and further study of M2N, Zhang et al. (2024) introduced Universal Mesh Movement Network (UM2N), which consists of an encoder based on a Graph Transformer and a decoder based on a GAT. Compared to the previous M2N, it selects the element volume loss as training loss instead of the coordinates loss, which is driven by the need for greater physical validity and robustness in automated mesh adaptation. This significantly improves the speed of mesh generation, robustness, and capability of adaptive meshing to address complex boundary problems (following the results in Zhang et al. (2024)). However, the complexity of the existing experiments with these methods is still far removed from real-life applications including coastal tsunami modelling.

This work extends research on UM2N (Zhang et al., 2024) and traditional MA based mesh movement (McRae et al., 2018; Clare et al., 2021), and further develops non-hydrostatic modelling within the Thetis framework (Pan et al., 2019, 2021). It also represents the first demonstration of a DG-FE based PDE solver integrated with UM2N (AI for mesh adaptation), applied to non-hydrostatic shallow water equations for the simulation of coastal tsunami propagation and run-up with significant water dispersion.

The remainder of this paper is organized as follows. Sect. 2 describes the mathematical derivation of the governing equations including the underlying non-hydrostatic ocean model, and the treatment of the wet-dry interface. Advanced discretisation approaches within Thetis' PDE solver and mesh adaptation methods are described in Sect. 3 and Sect. 4, respectively. Sect. 5 describes a series of test cases that are used for model verification and validation. Conclusions are presented and results are discussed in Sect. 6.

2. Mathematical formulation 116

2.1. Governing equations of non-hydrostatic model 117

In this study, a single-layer non-hydrostatic free surface model is adopted 118
for our simulations. The total water depth, denoted by H [m], satisfies: 119

$$H = \eta + b, \quad (1)$$

where η [m] is the free surface elevation and $b = b(\mathbf{x})$ [m] is the bathymetry. 120

Although the flow is assumed to be hydrostatic in many ocean models, 121
the effects of wave dispersion can play a significant role in the process of 122
nearshore wave evolution, such as wave propagation on a sloping beach. It is 123
therefore sometimes necessary to consider non-hydrostatic effects caused by 124
water dispersion in the modelling of shoreward wave propagation (Pan et al., 125
2019). This means that the vertical acceleration may not be ignored. Under 126
the non-hydrostatic condition, the total pressure can be decomposed into a 127
hydrostatic pressure part p_h and a non-hydrostatic part q (cf., e.g., Pan et al. 128
(2019) and Stelling and Zijlema (2003)): 129

$$p = p_h + q, \quad (2)$$

with the hydrostatic pressure written as: 130

$$\frac{\partial p_h}{\partial z} = \rho g \quad \implies \quad p_h = p_a + \rho g(\eta - z), \quad (3)$$

where p_a is the atmospheric pressure, ρ is the density of the fluid of interest 131
(i.e. sea water) and g is the gravitational acceleration. 132

The 3D Navier-Stokes momentum equations in non-conservative form can 133
be expressed as: 134

$$\nabla_h \cdot \mathbf{u} + \frac{\partial w}{\partial z} = 0, \quad (4)$$

$$\begin{aligned} \frac{\partial \mathbf{u}}{\partial t} + \mathbf{u} \cdot \nabla_h \mathbf{u} + w \frac{\partial \mathbf{u}}{\partial z} + F_c \mathbf{e}_z \times \mathbf{u} + \frac{1}{\rho} \nabla_h p \\ + \frac{C_d \|\mathbf{u}\| \mathbf{u}}{H} = \nabla_h \cdot (\nu \nabla_h \mathbf{u}) + \frac{\partial}{\partial z} \left(\nu \frac{\partial \mathbf{u}}{\partial z} \right) + \mathbf{S}_H, \end{aligned} \quad (5)$$

$$\frac{\partial w}{\partial t} + \mathbf{u} \cdot \nabla_h w + w \frac{\partial w}{\partial z} + \frac{1}{\rho} \frac{\partial p}{\partial z} + g = \nabla_h \cdot (\nu \nabla_h w) + \frac{\partial}{\partial z} \left(\nu \frac{\partial w}{\partial z} \right) + S_V, \quad (6)$$

where \mathbf{u} is the velocity in the horizontal direction and ∇_h denotes the horizontal 135
 gradient operator. In addition, F_c [Hz], C_d (dimensionless) and ν [m^2s^{-2}] 136
 are Coriolis parameter, quadratic drag coefficient and kinematic viscosity res- 137
 pectively. They are used to describe three external and body forces: Coriolis 138
 effect, bottom friction and viscosity respectively (Kärnä et al., 2018; Wall- 139
 work, 2021). \mathbf{S}_H denotes other source terms in the horizontal directions such 140
 as wind stress and rainfall intensity. Finally, w and S_V denote velocity and 141
 source terms in the vertical direction, respectively. 142

The kinematic boundary condition at the free surface, $z = \eta(x, y, t)$, and 143
 an impermeable land condition at the bottom, $z = -b(x, y)$, are expressed 144
 as (Pan et al., 2019): 145

$$w|_{z=\eta} = \frac{\partial \eta}{\partial t} + \mathbf{u}|_{z=\eta} \cdot \nabla_h \eta, \quad (7)$$

$$w|_{z=-b} = -\mathbf{u}|_{z=-b} \cdot \nabla_h b. \quad (8) \quad 146$$

Using the two boundary conditions above, the mass continuity equation 147
 in the non-conservative form is obtained via integrating Eq. 4 over the depth: 148

$$\frac{\partial \eta}{\partial t} + \nabla_h \cdot (H\bar{\mathbf{u}}) = 0, \quad \text{with} \quad \bar{\mathbf{u}} = \frac{1}{H} \int_{-b}^{\eta} \mathbf{u} dz, \quad (9)$$

where $\bar{\mathbf{u}}$ denotes the depth-averaged horizontal velocity. Then, Eq. 2 and 149
 Eq. 3 are substituted into Eq. 5, and Eq. 5 is integrated over water depth 150
 H , the depth-averaged horizontal momentum equation, neglecting vertical 151
 advection and viscosity terms, can be written as: 152

$$\frac{\partial \bar{\mathbf{u}}}{\partial t} + \bar{\mathbf{u}} \cdot \nabla_h \bar{\mathbf{u}} + F_c \mathbf{e}_z \times \bar{\mathbf{u}} + g \nabla_h \eta + \frac{1}{\rho H} \int_{-b}^{\eta} \nabla_h q dz = \bar{\mathbf{F}}_H + \bar{\mathbf{V}}_H + \bar{\mathbf{S}}_H, \quad (10)$$

with

$$\bar{\mathbf{F}}_H = -\frac{C_d \|\bar{\mathbf{u}}\| \bar{\mathbf{u}}}{H} \quad \text{and} \quad \bar{\mathbf{V}}_H = \frac{1}{H} \nabla_h \cdot (H\nu \nabla_h \bar{\mathbf{u}}), \quad 153$$

where $\bar{\mathbf{F}}_H$ is the bottom friction term, where the coefficient C_d is used to 154
 describe a dimensionless bottom friction coefficient. $\bar{\mathbf{V}}_H$ is the horizontal 155
 viscosity term, and $\bar{\mathbf{S}}_H$ represents any other source terms, such as wind stress. 156
 Following Pan et al. (2019) and Stelling and Zijlema (2003), the vertical 157
 integral of the non-hydrostatic pressure gradient can be expressed by applying 158

the Leibniz integral rule and linear average approximation:

159

$$\begin{aligned} \int_{-b}^{\eta} \nabla_h q \, dz &= \nabla_h \int_{-b}^{\eta} q \, dz - q|_{z=-b} \nabla_h b \\ &\approx \nabla_h \left(\frac{1}{2} q H \right) - q|_{z=-b} \nabla_h b \\ &= \frac{1}{2} H \nabla_h q + \frac{q}{2} \nabla_h (\eta - b). \end{aligned}$$

Substituting the approximation above into Eq. 10. The depth-average momentum equation in horizontal dimension is:

160

161

$$\frac{\partial \bar{\mathbf{u}}}{\partial t} + \bar{\mathbf{u}} \cdot \nabla_h \bar{\mathbf{u}} + F_c \mathbf{e}_z \times \bar{\mathbf{u}} + g \nabla_h \eta + \frac{1}{2} \frac{\nabla_h q}{\rho} + \frac{1}{2} \frac{q}{\rho H} \nabla_h (\eta - b) = \bar{\mathbf{F}}_H + \bar{\mathbf{V}}_H + \bar{\mathbf{S}}_H. \quad (11)$$

For the vertical dimension, the terms of vertical advection and viscosity are neglected since they are generally small than the vertical non-hydrostatic pressure gradient (Pan et al., 2019). Following Pan et al. (2019) and Stelling and Zijlema (2003), the vertical velocity w is approximated as a linear profile based on the Keller-box scheme. Therefore, the vertical momentum Eq. 6 for shallow water can be written as:

162

163

164

165

166

167

$$\frac{\partial w}{\partial t} + \frac{1}{\rho} \frac{\partial q}{\partial z} = \frac{\partial}{\partial t} \left(\frac{w|_{z=\eta} + w|_{z=-b}}{2} \right) + \frac{q}{H} = 0. \quad (12)$$

Additionally, one more equation is required to close the system since there are two new variables, q and w added to the system. Hence the 3D continuity Eq. 4 is expressed as:

168

169

170

$$\nabla_h \cdot \mathbf{u} + \frac{w|_{z=\eta} - w|_{z=-b}}{H} = 0. \quad (13)$$

In summary, Eq. 9 and Eqs. 11–13 constitute the governing equations for the depth-integrated non-hydrostatic model. It is noted that Eq. 11 would yield the hydrostatic NSWE if $q = 0$. This means this depth-integrated non-hydrostatic model can be considered the extension of the hydrostatic model under 2D conditions with one layer (Pan et al., 2019). The functionality and transform between non-hydrostatic and hydrostatic are implemented in Thetis (Kärnä et al., 2018) and available through a configuration option.

171

172

173

174

175

176

177

2.2. *Governing equations for a wet-dry domain* 178

In many coastal ocean problems, a wet-dry interface is involved in the simulation of wave propagation, e.g., where a wave generated by tsunami moves to nearshore from a wet domain to a dry domain. Following the wetting-and-drying formulation of Kärnä et al. (2011) and Kärnä et al. (2018) in Thetis, the modified total water depth can be expressed as: 179
180
181
182
183

$$\tilde{H} := H + f(H), \quad (14)$$

where $f(H) := (\sqrt{H^2 + \alpha^2} - H)/2$ is defined as a smooth function to ensure positive water depth. Analogously, the function of bathymetry is also redefined and written as: 184
185
186

$$\tilde{b} = b + f(H). \quad (15)$$

Hence, the governing equations of depth-integrated non-hydrostatic model are modified in the following way by taking the wetting-drying effect into account: 187
188
189

$$\frac{\partial \eta}{\partial t} + \frac{\partial \tilde{b}}{\partial t} + \nabla_h \cdot (\tilde{H} \bar{\mathbf{u}}) = 0, \quad \text{with} \quad \bar{\mathbf{u}} = \frac{1}{\tilde{H}} \int_{-\tilde{b}}^{\eta} \mathbf{u} dz. \quad (16)$$

$$\frac{\partial \bar{\mathbf{u}}}{\partial t} + \bar{\mathbf{u}} \cdot \nabla_h \bar{\mathbf{u}} + F_c \mathbf{e}_z \times \bar{\mathbf{u}} + g \nabla_h \eta + \frac{1}{2} \frac{\nabla_h q}{\rho} + \frac{1}{2} \frac{q}{\rho \tilde{H}} \nabla_h (\eta - \tilde{b}) = \bar{\mathbf{F}}_H + \bar{\mathbf{V}}_H + \bar{\mathbf{S}}_H, \quad (17)$$

with 190

$$\bar{\mathbf{F}}_H = -\frac{C_d \|\bar{\mathbf{u}}\| \bar{\mathbf{u}}}{\tilde{H}} \quad \text{and} \quad \bar{\mathbf{V}}_H = \frac{1}{\tilde{H}} \nabla_h \cdot (\tilde{H} \nu \nabla_h \bar{\mathbf{u}}).$$

The depth-average momentum equation in vertical dimension can be written as: 191
192

$$\frac{\partial w}{\partial t} + \frac{1}{\rho} \frac{\partial q}{\partial z} = \frac{\partial}{\partial t} \left(\frac{w|_{z=\eta} + w|_{z=-\tilde{b}}}{2} \right) + \frac{q}{\tilde{H}} = 0, \quad (18)$$

and Eq. 13 (Eq. 6) is modified as: 193

$$\nabla_h \cdot \mathbf{u} + \frac{w|_{z=\eta} - w|_{z=-\tilde{b}}}{\tilde{H}} = 0. \quad (19)$$

In summary, Eqs. 16–19 form the governing equations for the depth-integrated non-hydrostatic model with wetting-drying impact. More details of this model can be found in the works of Pan et al. (2019) and Clare et al. (2021). The main difference between the standard formulation and the wetting-drying type is a mass correction term because of the moving bathymetry (See the second term of Eq. 16). This functionality is available through a configuration option in Thetis (Kärnä et al., 2018). 194
195
196
197
198
199
200

3. Discretization methods and implementation in Thetis and Firedrake

The non-hydrostatic model is solved using the unstructured-mesh finite element coastal ocean modelling system, Thetis (Kärnä et al., 2018), which is built upon the automated code generation framework, Firedrake (Ham et al., 2023). Following the pioneering work and relevant extensions of layer-averaged non-hydrostatic approach (Stelling and Zijlema, 2003; Wei and Jia, 2013) and non-hydrostatic pressure correction (Marshall et al., 1997; Stansby and Zhou, 1998; Lai et al., 2010), Pan et al. (2019) integrated the layer-averaged non-hydrostatic approach into DG finite element implementation in Thetis. In this formulation the 3D incompressible Navier–Stokes (NS) equations are vertically integrated to obtain a depth-averaged continuity equation for total water depth H , and a horizontal momentum equation for the depth-averaged velocity $\bar{\mathbf{u}}$. Mentioned in Sect. 2, non-hydrostatic effects are represented by decomposing the pressure into hydrostatic and non-hydrostatic parts and retaining a depth-averaged non-hydrostatic pressure q in the horizontal momentum balance. The vertical momentum and continuity equations are combined to yield a Poisson problem in the depth-integrated (Pan et al., 2019).

In the spatial discretisation, the depth-averaged variables (free-surface elevation and horizontal velocity) are discretised on unstructured triangular meshes with a discontinuous Galerkin (DG) finite element formulation, typically piecewise linear $\mathbb{P}_1^{DG} - \mathbb{P}_1^{DG}$ spaces. Numerical fluxes across element interfaces are treated using linearised approximate Riemann solvers, and viscosity is stabilised by an interior-penalty formulation (Kärnä et al., 2018). The discrete weak forms are implemented in the high-level Unified Form Language (UFL) within the Firedrake code-generation framework, and the resulting discretised equations are solved using linear solvers available through the PETSc library (Balay et al., 2025; Dalcin et al., 2011). The implementation ensures the non-hydrostatic extension is fully consistent with the existing hydrostatic solver in Thetis, and preserves the properties of high-order convergence and numerical stability of the original hydrostatic DG code (follow the work of Pan et al. (2019)).

Temporal discretisation follows a split-step pressure-correction strategy: in the initial hydrostatic step the free-surface elevation and depth-averaged velocity are advanced using an implicit θ -scheme (i.e., Crank–Nicolson with $\theta = 0.5$) for the free surface and pressure-gradient terms, with advection and

other source terms treated explicitly (Pan et al., 2019). In the subsequent non-hydrostatic correction step, the intermediate velocities obtained from the hydrostatic step (not yet divergence-free) are adjusted, which is achieved by solving the Poisson equation for the non-hydrostatic pressure q (Pan et al., 2019; Cui et al., 2014). The solution to this equation is then used to correct the horizontal and vertical velocities, effectively projecting them onto a divergence-free field that strictly enforces the 3D continuity equation. These two steps allow the model to accurately represent the characteristics of dispersive waves, while maintaining the stability and efficiency of the underlying hydrostatic framework (Pan et al., 2019).

4. Universal Mesh Movement Network (UM2N)

4.1. Monge–Ampère mesh movement

Following the work of McRae et al. (2018), Wallwork (2021) and Zhang et al. (2024), the mesh movement process can be defined as the optimization process to find the transformation between a computational domain, Ω_C , and a physical domain, Ω_P . The aim of mesh movement is to obtain the mapping $\mathbf{x}(\boldsymbol{\xi}) : \Omega_C \rightarrow \Omega_P$, such that the provided monitor function $m(\mathbf{x})$ satisfies an equidistribution condition. It leads to the optimization problem that can be expressed as (Wallwork, 2021):

$$\min_{\mathbf{x}:\Omega_C \rightarrow \Omega_P} \|\mathbf{x}(\boldsymbol{\xi}, t) - \boldsymbol{\xi}\|_{L^2(\Omega_C)} \quad \text{subject to} \quad m(\mathbf{x}) \det \mathbf{J} = \theta, \quad (20)$$

where $\boldsymbol{\xi}$ are the computational coordinates. \mathbf{J} denotes the Jacobian of the mapping $\mathbf{x}(\boldsymbol{\xi})$, and θ is a normalisation constant:

$$\mathbf{J}_{ij} := \frac{\partial x_i}{\partial \xi_j} \quad \text{and} \quad \theta := \frac{\int_{\Omega_P} m dx}{\int_{\Omega_C} d\xi}. \quad (21)$$

According to Brenier (1991) and Delzanno et al. (2008), the optimisation problem Eq. 20 can be constrained to have a unique solution by using optimal transport theory, where the deformation of the mapping is expressed in the following form:

$$\mathbf{x}(\boldsymbol{\xi}) = \boldsymbol{\xi} + \nabla_{\boldsymbol{\xi}} \Phi(\boldsymbol{\xi}), \quad (22)$$

where Φ denotes a scalar potential. This deformation form, Eq. 22, ensures that the quantity $\Phi + \frac{1}{2}|\boldsymbol{\xi}^2|$ is convex, which in turn guarantees that the

mapping is injective (Brenier, 1991; McRae et al., 2018). Substituting Eq. 22 into Eq. 20, a nonlinear PDE of Monge–Ampère (MA) type is obtained:

$$m(\mathbf{x}) \det(\mathbf{I} + \mathbf{H}(\Phi)) = \theta, \quad \text{where} \quad \mathbf{H}(\Phi)_{ij} := \frac{\partial^2 \Phi}{\partial \xi_i \partial \xi_j} \quad (23)$$

is the Hessian of Φ and \mathbf{I} is the identity matrix.

Notice that the MA type equation (Eq. 23) is an auxiliary PDE which is only associated with the process of mesh movement, independent of the governing PDE equations or physical problems to solve (Zhang et al., 2024). This means that, although the specific choice of monitor function may be guided by the physical problem (see the following section), the form of the MA equation is invariant across different PDEs. As argued by Zhang et al. (2024), this decoupling enhances the generalization of machine learning based mesh movement methods, i.e., a trained MA neural solver can transfer to new scenarios with a low cost of fine-tuning, or without retraining.

4.2. Design of Monitor function

4.2.1. Monitor function choice

Following Wallwork (2021), the Hessian of a solution field is adopted to constitute the monitor function. This is because it introduces information about curvature, which is crucial for accurately resolving transitions in the solution field. Specifically, curvature information is obtained from the point-wise Frobenius norm of the Hessian $\|\mathbf{H}\|$ (Clare et al., 2021; Wallwork, 2021). In this study, the Hessian \mathbf{H} which is used in UM2N is directly computed from the numerical solution of the elevation η_h . The monitor function based on the Frobenius norm of the Hessian matrix can be written as:

$$m := 1 + \alpha \frac{\|\mathbf{H}(\eta_h)\|}{\max \|\mathbf{H}(\eta_h)\|}, \quad \alpha > 0, \quad \text{where} \quad \|\mathbf{H}\| = \sqrt{\sum_{i=1}^2 \sum_{j=1}^2 \mathbf{H}_{ij}}. \quad (24)$$

Here, α is a user-specified parameter, which in this work is set as $\alpha = 5$.

Further modifications to the monitor function are introduced in Sect. 5.3, following the work in Clare et al. (2021), to better resolve the wetting-drying interface.

4.2.2. Monitor smoothness

Wallwork (2021) also mentioned that applying monitor functions based on the Hessian (or gradient) may lead to non-smoothness issues, particularly if the function became too focused on sharp interfaces. To generate adaptive meshes with greater regularity and uniformity, smoothing of the monitor function is performed before mesh movement at each timestep.

A widely used numerical procedure for the smoothing of a scalar function is through the discretisation of a diffusion equation, e.g. the heat equation:

$$\frac{\partial m(\mathbf{x})}{\partial t} = \kappa \nabla^2 m(\mathbf{x}). \quad (25)$$

We consider a standard Continuous Galerkin finite element discretisation in combination with an implicit Euler time discretisation. A single (pseudo) time step takes the following form:

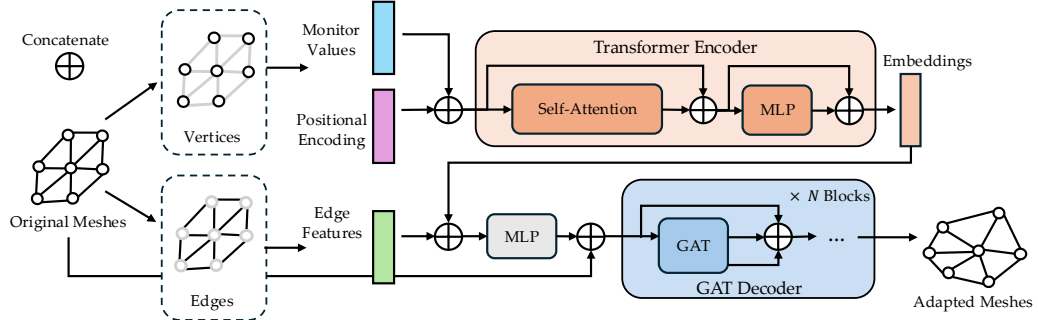
$$\int_{\Omega} \phi_m \cdot \tilde{m} \, d\mathbf{x} - \int_{\Omega} \phi_m \cdot m \, d\mathbf{x} + \tilde{\alpha} \int_{\Omega} (\mathbf{J} \cdot \nabla \phi_m) \cdot (\mathbf{J} \cdot \nabla \tilde{m}) \, d\mathbf{x} = 0. \quad (26)$$

For all test functions ϕ_m in the discrete function space V , the same as used for discretizing the monitor function $m(x)$, here the space of piecewise linear functions with values at the vertex nodes. We have inserted the Jacobian \mathbf{J} of the transformation between reference element and physical element, to transform the physical space derivative, ∇ , to a derivative with respect to reference coordinates. This ensures that the diffusion coefficient $\tilde{\alpha}$, which controls the length scale over which the monitor is diffused, is expressed relative to the local grid size. For a constant value of $\tilde{\alpha}$ the smoothing occurs over the same number of grid lengths, even where the mesh is anisotropic.

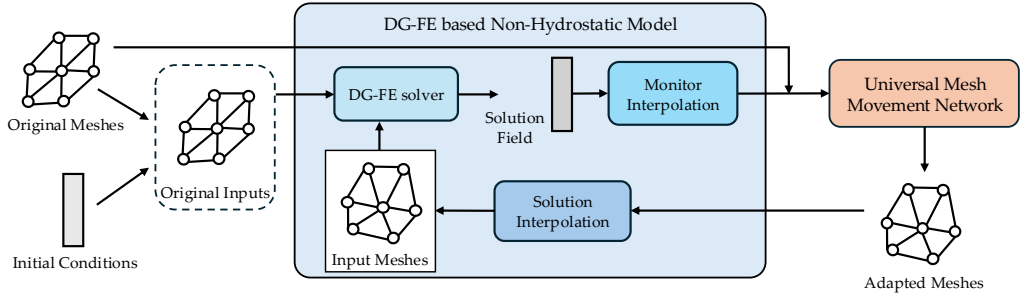
Starting from the given monitor function, e.g., based on (24), as the initial condition $m(x)$, we perform a single (pseudo) time step by solving (26) for \tilde{m} . The value of diffusion coefficient $\tilde{\alpha}$ is set from 0.3 to 0.5 when performing the monitor smoothing for test cases. In this way, for each timestep $t^{(k)}$, the monitor function $m^{(k)}$ is smoothed to obtain $\tilde{m}^{(k)}$ which is then fed into the UM2N-based mesh movement.

4.3. UM2N framework

The UM2N framework, introduced in Zhang et al. (2024), mainly consists of a Graph Transformer encoder and a Graph Attention Network (GAT) based decoder. The graph transformer encoder is used as a feature extractor. The original mesh coordinates, $\boldsymbol{\xi}$, and monitor values evaluated at these



(a) Universal Mesh Movement Network (UM2N) Framework



(b) UM2N based PDE solver Framework

Figure 1: Overview of Universal Mesh Movement Network (UM2N) shown in (a), cited from Zhang et al. (2024), and UM2N based PDE solver pipeline shown in (b). The monitor interpolation in (b) includes a step of monitor smoothing.

coordinates, $m(\xi)$, are set as the input features, in which the coordinates 322
serve as the positional encoding, and features are concatenated and encoded 323
into \mathbf{Q} (Query), \mathbf{K} (Key) and \mathbf{V} (Value) matrices via Multi-Layer Perceptrons 324
(MLPs) for a self-attention module. The embedding \mathbf{z} are generated by the 325
encoder as output, which are fed into a subsequent GAT based deformer for 326
mesh movement (Zhang et al., 2024). 327

A Graph Attention Network (GAT) is adopted as the decoder in UM2N, 328
chosen for its ability to restrict vertex movement to within a single hop of 329
neighboring vertices, thereby alleviating mesh tangling issues. The decoder 330
comprises N GAT blocks, where the initial block receives the mesh query ξ , 331
the embeddings \mathbf{z} from the encoder part, and the edge features \mathbf{e} as inputs. 332
For each subsequent k^{th} block, the inputs include the coordinates of the initial 333
mesh ξ , the coordinates of the moved mesh $\xi^{(k-1)}$ and the extracted features 334

from the previous $(k - 1)^{th}$ block (Zhang et al., 2024). 335

In summary, the input mesh vertex and edge features are collected, with 336
vertex coordinates and monitor function values processed by a graph trans- 337
former to generate embeddings. These embeddings, combined with edge 338
features, are fed into a Graph Attention Network (GAT) decoder, which, 339
along with a mesh query, produces the adapted meshes. 340

For the training of UM2N, a PDE-independent training dataset, $D = \{\mathbf{d} :$ 341
 $\mathbf{d} = (\boldsymbol{\xi}, m_{\boldsymbol{\xi}}; \mathbf{V}_r, \mathbf{K}_r)\}$, is constructed by original mesh coordinates $\boldsymbol{\xi}$, monitor 342
values $m_{\boldsymbol{\xi}}$, the coordinates of pre-calculated (reference) mesh’s nodes \mathbf{V}_r and 343
elements \mathbf{K}_r . The dataset is generated by randomly creating generic solution 344
fields, each formed by summing a random number of Gaussian distribution 345
functions centered at random locations with random widths in different di- 346
rections to incorporate anisotropy (see Figure A1 and Appendix B in Zhang 347
et al. (2024)). These generated fields are designed to be interpretable as 348
solutions of arbitrary PDEs. 349

4.4. Loss functions 350

Following the notation of Zhang et al. (2024), the adapted mesh can 351
be denoted as $\mathcal{H}_a(\boldsymbol{\xi}, m_{\boldsymbol{\xi}}; \boldsymbol{\theta}) = \{\mathbf{V}_a, \mathbf{K}_a\}$, where $\boldsymbol{\theta}$ is the model parameters 352
of UM2N, $\mathbf{V}_a = \{\mathbf{x}_i\}_{i=1}^{N_1}$ denotes the arrays of vertex coordinates in the 353
adapted meshes, and $\mathbf{K}_a = \{\mathbf{k}_i\}_{i=1}^{N_2}$ denotes the set of elements with x_i as 354
the i^{th} vertex in the adapted meshes. Similarly, $\mathbf{y}_i, \mathbf{q}_i$ are used to represent 355
the coordinates of the i^{th} vertex and element respectively in sets \mathbf{V}_r and \mathbf{K}_r 356
for the reference meshes. 357

Given the dataset D , defined in the previous section, the final objective is 358
to find model parameters $\boldsymbol{\theta}$, by minimizing the total loss, \mathcal{L} , that consists of 359
the element volume loss, \mathcal{L}_{vol} , and Chamfer distance loss, \mathcal{L}_{cd} (Zhang et al., 360
2024). This process can be expressed as: 361

$$\arg \min_{\boldsymbol{\theta}} \mathcal{L}(\boldsymbol{\theta}) := \lambda_{vol} \mathcal{L}_{vol}(\boldsymbol{\theta}) + \lambda_{cd} \mathcal{L}_{cd}(\boldsymbol{\theta}), \quad \lambda_{vol}, \lambda_{cd} > 0, \quad (27)$$

where λ_{vol} and λ_{cd} represent hyper-parameters used to balance these two 362
effects. 363

The element volume loss is obtained by computing the averaged volume 364
difference between each element in the adapted meshes (\mathbf{K}_a) and that in 365
reference meshes (\mathbf{K}_r) obtained from the MA movement (Zhang et al., 2024). 366

The loss is then expressed as:

$$\mathcal{L}_{vol}(\boldsymbol{\theta}) = \mathbb{E}_{(\boldsymbol{\xi}, m_{\boldsymbol{\xi}}; \mathbf{V}_r, \mathbf{K}_r) \in D} \left[\frac{1}{|\mathbf{K}_a|} \sum_{i=1}^{N_2} |\text{Vol}(\mathbf{k}_i) - \text{Vol}(\mathbf{q}_i)| \right], \quad (28)$$

where $\text{Vol}(\cdot)$ is the volume (area) of a given element.

The Chamfer distance loss is obtained by computing the Chamfer distance that finds the nearest distances for each node between adapted meshes and reference meshes and then sums the square of the distances (Zhang et al., 2024). It can be expressed as:

$$\begin{aligned} \mathcal{L}_{cd}(\boldsymbol{\theta}) = \mathbb{E}_{(\boldsymbol{\xi}, m_{\boldsymbol{\xi}}; \mathbf{V}_r, \mathbf{K}_r) \in D} & \left[\frac{1}{|\mathbf{V}_a|} \sum_{\mathbf{x}_i \in \mathbf{V}_a} \min_{\mathbf{y}_j \in \mathbf{V}_r} \|\mathbf{x}_i - \mathbf{y}_j\|_2 \right. \\ & \left. + \frac{1}{|\mathbf{V}_r|} \sum_{\mathbf{y}_j \in \mathbf{V}_r} \min_{\mathbf{x}_i \in \mathbf{V}_a} \|\mathbf{x}_i - \mathbf{y}_j\|_2 \right]. \end{aligned} \quad (29)$$

This metric encourages the model to produce meshes with a spatial distribution of nodes closely resembling that of the reference meshes. Unlike applications in three-dimensional reconstruction or computer vision where Chamfer distance might be calculated by sampling thousands of random points from a continuous surface to compare shapes, UM2N adopts the bidirectional Chamfer distance shown in Eq. 29, which operates directly on the discrete vertices of the meshes without requiring additional sampling.

4.5. UM2N based PDE solver

Fig. 1 shows the UM2N-based PDE solver framework, which consists of UM2N itself (Fig. 1 (a)) which is incorporated in the DG-FE based Non-Hydrostatic solver loop (Fig. 1 (b)). The network of UM2N is trained exclusively on the values of the monitor function, which can be computed relatively efficiently from the PDE solution. The desired movement of mesh nodes is determined by solving the Monge–Ampère equation for each monitor function, which is derived from randomly generated PDE solutions. Following the training process, the model can be deployed using only the monitor values as input, thereby functioning independently of the specific PDE being solved.

In Fig. 2, a schematic diagram further illustrates the solution process of one timestep within the UM2N based PDE solver pipeline. At timestep $t^{(i)}$, one general iteration starts from the adapted mesh $\mathcal{H}_a^{(i-1)}$ together with the

blue and green background panels in Fig. 2.)

411

5. Model Verification and Validation

412

5.1. N-wave strip source

413

This problem was introduced in Kanoğlu et al. (2013) as an idealised model for tsunami propagation studies, and is based on a finite strip source over a constant bathymetry solved using the linear shallow water equation. This test case is used here to investigate the convergence, robustness and accuracy-cost balance for UM2N, compared to Monge–Ampère (MA) based mesh movement. The computational domain is given by $\Omega = [-100, 100] \times [-100, 100]$ with open boundaries. According to Kanoğlu et al. (2013) and

420

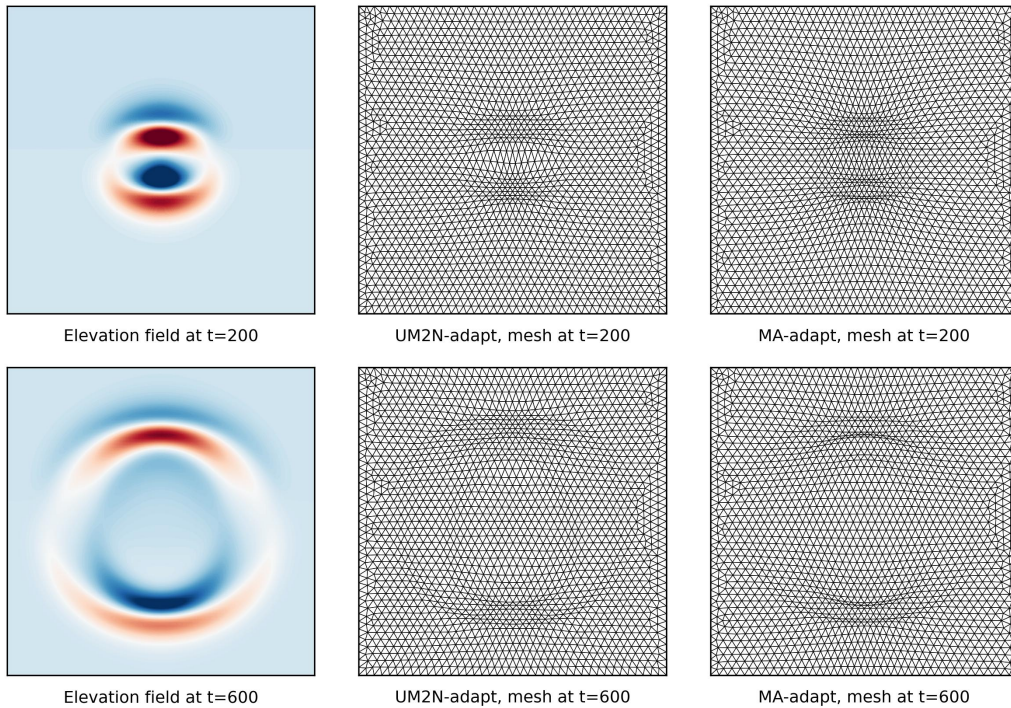


Figure 3: Comparison of N-wave test case: Two-dimensional plan view of wave patterns after propagating at $t = 200$ (upper left) and $t = 600$ (bottom left), and their corresponding meshes via different mesh configurations: MA movement (middle column) and UM2N (right column). The scale of elevation range for 2D plan view (left column) is from -0.5×10^{-4} to 0.75×10^{-4} shown by blue to red.

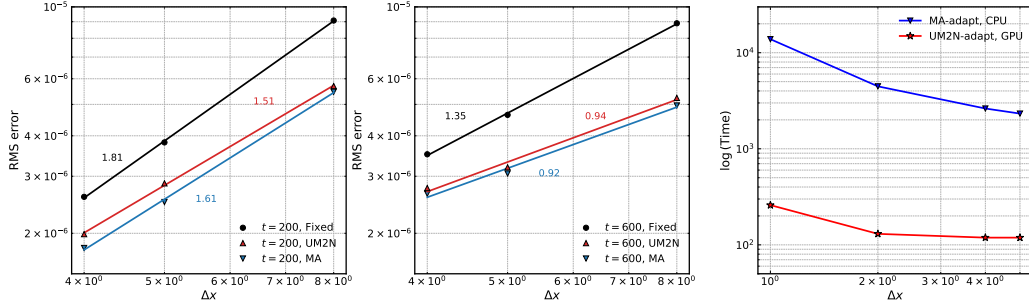


Figure 4: Convergence of RMS error of free-surface elevations in the N-wave strip source test case for fixed meshes, MA moved meshes and UM2N moved meshes at times $t=200$ (left) and $t=600$ (middle), respectively. Comparisons of computational cost (average inference time of mesh adaptation on CPU/GPU) for fixed meshes, MA meshes and UM2N meshes (right). Mesh sizes correspond to $\Delta x = 8.0, 5.0,$ and 4.0 m in convergence plots at left and middle columns, and $\Delta x = 5.0, 4.0, 2.0$ and 1.0 m in plot of computational cost at right column. The numbers show the slope of the least-squares fitted linear lines (black: fixed meshes; blue: MA moved meshes; red: UM2N moved meshes).

Tadepalli and Synolakis (1994), the initial elevation of N-wave type is defined as: 421
422

$$\eta_0(x, y) = \frac{\epsilon H}{2} \left[\tanh(\gamma_n(x - x_0)) - \tanh(\gamma_n(x - x_0 - L)) \right] (y - y_2) \operatorname{sech}^2(\gamma_n(y - y_1)), \quad (30)$$

where ϵ is a scaling parameter and H is the initial wave height measured from the bottom topography to the free surface. In Eq.30, x_0 and L are the starting point and crest length of the source, respectively. In addition, y_1 and y_2 are the locations of depression and elevation for an N-wave, respectively. Furthermore, the steepness of the wave is denoted as p_0 in the parameter $\gamma_n = \sqrt{3Hp_0}/4$. 423
424
425
426
427
428

In the presented computations, these parameters are set to $\epsilon = -0.04$, $H = 0.001$, $x_0 = -15$, $L = 30$, $y_1 = 0$, $y_2 = 2.3$ and $p_0 = 15$. The time duration of the simulation is $t_{end} = 600$. The analytical solution for this test case was derived in Kanoğlu et al. (2013). 429
430
431
432

Fig. 3 presents a comparison of results obtained using the UM2N adaptive mesh strategy against the MA movement for the N-wave strip source test case. The left column illustrates the 2D view of free-surface elevation at simulation times $t=200$ and $t=600$, showing the evolution from an initially 433
434
435
436

compact elevation-depression pair into a distinct, expanding circular wave structure. The corresponding mesh adaptation outcomes for UM2N and MA adaptations at these times are shown in the middle and right columns, respectively.

At the earlier time $t = 200$, the UM2N method primarily mobilizes mesh nodes locally, focusing refinements broadly around areas of corresponding significant wave peaks and troughs, while the MA movement generates tighter refinement regions, distributing nodes in a more structured and uniform manner (see the upper row of Fig. 3). This difference becomes more significant at $t = 600$, where UM2N continues to concentrate mesh refinement locally around the immediate vicinity of wave peaks and troughs. Additionally, the deformation of UM2N shows slight refinement in the area between the corresponding wave peaks and troughs, which results in obviously localized and somewhat noisy refinement. Mesh deformation obtained by MA movement continues to concentrate mesh refinement strictly around the immediate vicinity of wave peaks and troughs (follow the bottom row of Fig. 3).

Fig. 4 illustrates the convergence plot of the RMS errors for free-surface elevation in the N-wave strip source test case at two simulation stages, $t=200$ (left) and $t=600$ (middle), comparing fixed meshes, MA moved meshes and UM2N moved meshes with varying mesh resolutions. Even given the differences identified above between the two adapted meshes, both MA and UM2N mesh adaptation methods demonstrates improved accuracy, achieving lower RMS errors across all mesh resolutions compared to fixed meshes, although the results obtained using the UM2N approach show slightly less accuracy than that of the MA based mesh. Quantitative comparison of computational costs between MA and UM2N is also presented in Fig. 4. Computational inference time is recorded for a series of numerical experiments with different mesh resolutions. This demonstrates that using the UM2N method provides a speed-up of nearly 10^2 times compared with conventional MA movement, meaning that the UM2N method is able to significantly accelerate the process of mesh movement while achieving much of the accuracy improvement of the more costly MA method.

5.2. Solitary wave over a truncated conical shoal

This test case is designed to investigate our framework's abilities in simulating solitary wave run-up and refraction using the UM2N approach over a non-flat, wet bed bottom topography (see Fig. 5). The computational domain is set as $[0, 30] \text{ m} \times [0, 30] \text{ m}$ (see Fig. 6). A truncated conical-shaped

shoal is located at coordinates (12.96 m, 13.80 m). The shoal has a 0.25 m 474
height, and is submerged by 0.32 m-depth water initially. The non-flat part 475
of bottom topography is characterized by a truncated conical shoal, featuring 476
a top diameter of 2.60 m and a base diameter of 3.60 m. According to Nikolos 477
and Delis (2009) and Hou et al. (2013), the left boundary is set as the wave 478
inflow boundary where an input solitary wave with elevation η is defined by: 479

$$\eta(t) = A \operatorname{sech}^2 \left[\sqrt{\frac{3A}{4d^3}} C(t - T) \right], \quad (31)$$

where A denotes the amplitude of the wave and $C := \sqrt{g(A + d)}$ is the wave 480
celerity. A 5 m-wide sponge layer is located at the right outlet boundary. In 481
this numerical experiment, the ratio $A/d = 0.181$ is selected for numerical 482
validation and comparison of the MA and UM2N approaches. The resolution 483
of the coarse mesh is $\Delta x = 0.5$ m with Elevation degree of freedom count 484
(DOFs) totaling 25,296 and Velocity DOFs 50,592, while the resolution of 485
the fine mesh being $\Delta x = 0.25$ m with Elevation DOFs totaling 100,422 and 486
Velocity DOFs 200,844. The results obtained via both fixed coarse mesh 487
and fixed fine mesh have been used as a reference for those obtained on the 488
coarse mesh (Elevation DOFs = 100,422, and Velocity DOFs = 200,844), 489
with mesh adaptation approaches (i.e., UM2N and MA). The time step is 490
set to $\Delta t = 0.01$ s. 491

Fig. 7 presents the 2D contour of elevation and corresponding adapted 492
mesh when the solitary wave passes the shoal at different time instants, 493
 $t = 9.0, 11.0, 13.0$ s. Note that the traditional MA method fails (i.e., the solver 494

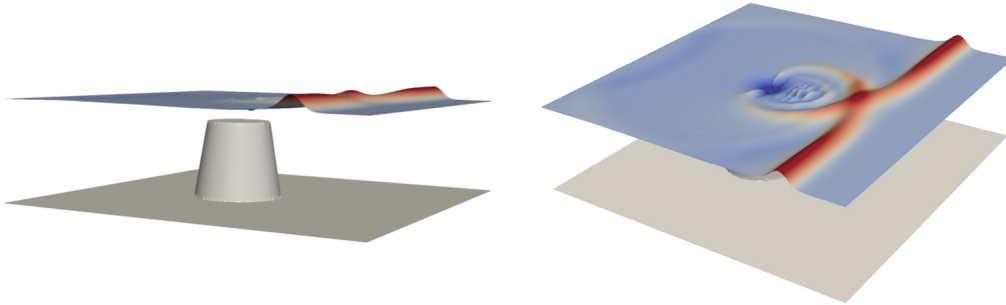


Figure 5: Three-dimensional view snapshots of wave patterns after propagating over a truncated conical shoal at $t = 15$ s, from different perspectives.

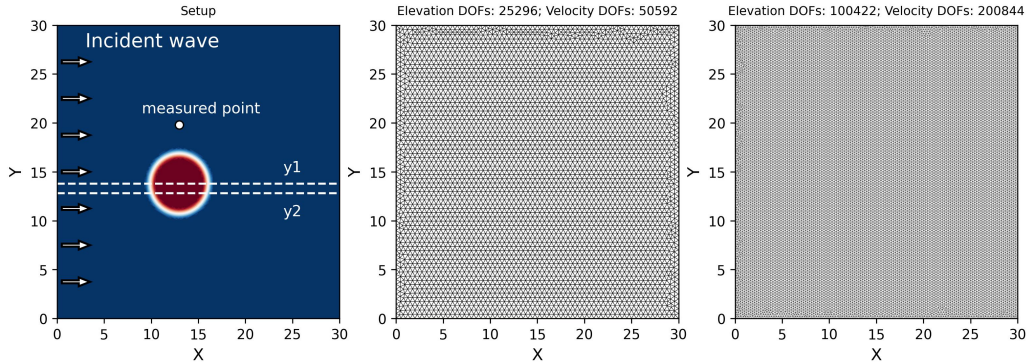


Figure 6: Conical shoal setup. Left: Two-dimensional plan view of bathymetry with measurement lines, measurement point (gauge) located at $(x = 12.96 \text{ m}, y = 19.80 \text{ m})$, and diagram of incident wave ($y_1 = 13.80 \text{ m}$, $y_2 = 12.80 \text{ m}$). Middle: coarse mesh topology. Right: fine mesh topology.

diverges) within 70~100 time steps in this scenario, due to mesh tangling or 495
 divergence in solving the MA equation. In general, UM2N based movement 496
 is able to track the incoming and refracting waves robustly over the whole 497
 time period considered. It shows agreement in capturing the whole solitary 498
 wave when passing the shoal. 499

Numerical comparisons between results of UM2N, fixed coarse mesh com- 500
 putations and fixed fine mesh are shown in Fig. 8. We find that the UM2N 501
 based adaptive simulation is able to better resolve free-surface behaviour in 502
 the cross sections than the fixed coarse mesh, especially in capturing the 503
 wave peaks (see top and middle rows in Fig. 8). Additionally, the time series 504
 elevation at the fixed measurement point indicates that UM2N based 505
 movement provides results that are closer to the fine mesh results while the 506
 fixed coarse mesh results deviate slightly in the timing of wave peak. This 507
 indicates that UM2N adaptive mesh also outperforms the fixed coarse mesh 508
 in tracking the independent solitary wave outside the shoal region. 509

5.3. Solitary wave over a conical island 510

This classical test case was introduced as a laboratory experiment and is 511
 used here to test the performance of each mesh adaptive approaches in terms 512
 of tracking wave run-up, refraction and reflection, under wetting-drying in- 513
 terface conditions (see Briggs et al. (1995), Lynett et al. (2002), Hou et al. 514

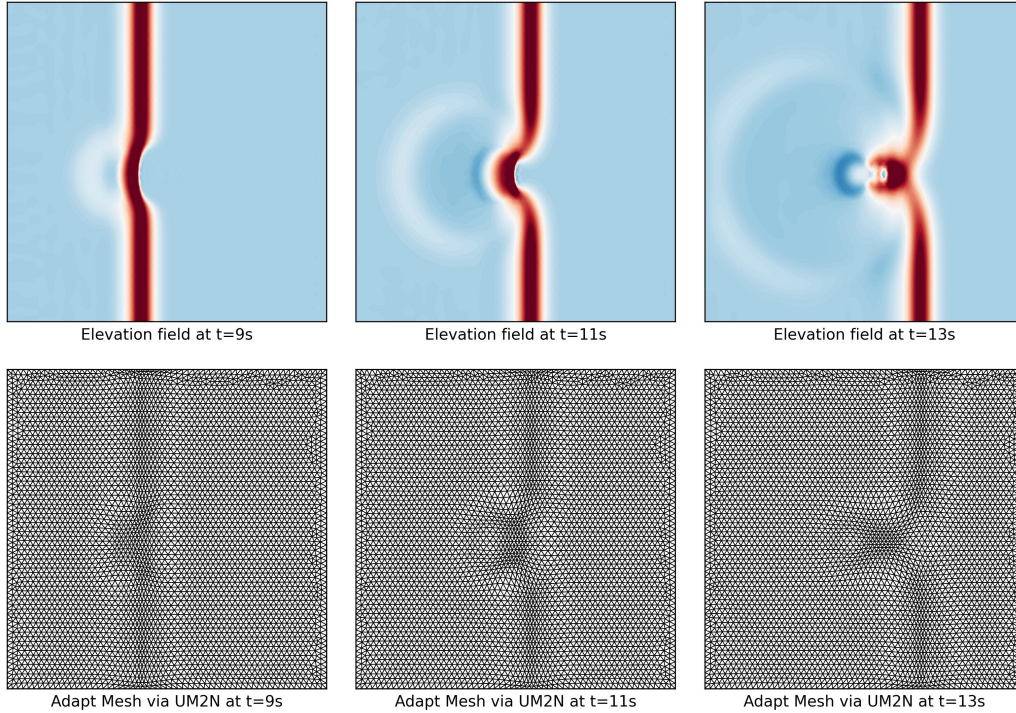


Figure 7: Top: Two-dimensional plan view of wave patterns when solitary wave passes the shoal at different time instants, $t = 9.0, 11.0, 13.0$ s. Corresponding adapted mesh using UM2N, performed on coarsened mesh. The scale of free surface elevation range is from -0.02 to 0.04 shown by blue to red.

(2013), Arpaia and Ricchiuto (2018) and Pan et al. (2019)). A truncated conical island is situated within a basin measuring 30 m long and 30 m wide. The island has a 0.625 m height, with its center located at coordinates (12.96 m, 13.80 m), and it is submerged by 0.32 m-depth water at the beginning. Its geometry is characterized by a truncated cone, featuring a top diameter of 2.2 m and a base diameter of 7.2 m. There is the same initial elevation with solitary wave type setup and boundary conditions (See Eq. 31) as the previous case.

We select the experiment with $A/d = 0.181$ as benchmark for numerical validation and comparison of the MA and UM2N approaches. A wet-dry interface occurs within the region of the initially submerged island, with significant gradients in both wave elevation and velocity fields resulting around

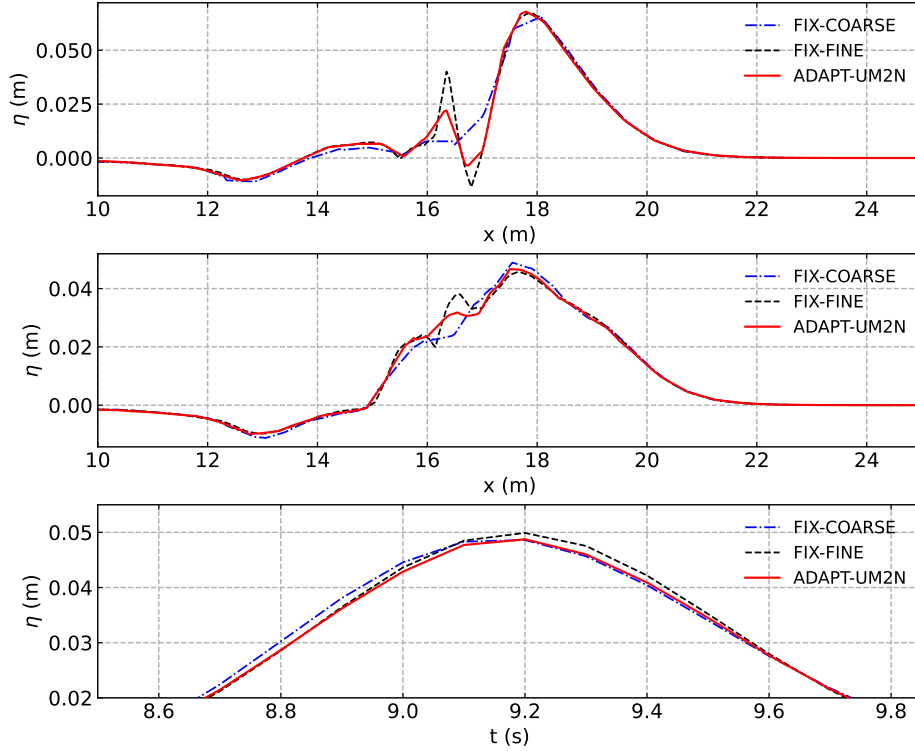


Figure 8: Numerical results comparison of results using UM2N on coarse mesh (red solid line), fixed coarse mesh computations (blue dashed line) and fixed fine mesh (black dashed line). Free-surface elevation in the cross sections at $t = 13$ s are presented in the top and middle rows (Top: y_1 -cross session; Middle: y_2 -cross session). Bottom: time series of free-surface elevation at fixed measured point.

the island. Hence, the configuration of the coarse meshes is such that higher mesh resolution is used with an element size $\Delta x = 0.3$ m in the vicinity of the island, while $\Delta x = 0.5$ m is adopted elsewhere, resulting in the number of elevation degree of freedoms (DOFs) being 50,439. Similarly, in this experiment, results obtained via both fixed coarse mesh and fixed fine mesh are used as a reference for those obtained via mesh adaptation approaches (i.e., UM2N and MA), on the coarse mesh with the same DOFs/mesh resolutions. The time step is set to $\Delta t = 0.01$ s. The coefficient of bottom friction is assumed to be 0.01, and horizontal viscosity is set as 0.015.

Instead of using the monitor function as in previous test cases 5.1–5.2, a

component that is designed to track the wet-dry interface is added. We also
 set the movement conditions via the monitor function in order to ensure that
 the mesh refinement has capability in tracking the movement of wave moves
 across the wet-dry interface and will not undergo additional redundant re-
 refinement at the dry domain when the wave passes over the wet-dry interface.
 The new monitor function is given by

$$m_\alpha(x, y) = \begin{cases} 1 + \mu \left(\alpha \frac{\min(\|H(\tilde{\eta})\|, H_{\max})}{H_{\max}} + \frac{\lambda}{\cosh(b_\lambda(\eta-b))^2} \right) & \text{if } \eta > -b, \\ 1 & \text{otherwise.} \end{cases} \quad (32)$$

where η is the free surface elevation, $\tilde{\eta} = \eta + f(H)$ is modified elevation ac-
 counting for the treatment of the wet-dry interface mentioned in Section 2.2,
 b is denotes as the bathymetry, b_λ controls the width of the wet-dry in-
 terface tracker (see Clare et al. (2021)), and the parameters μ , α and λ
 are all user-defined parameters. In the new monitor function, moreover,
 $H_{\max} = p_{\text{cap}} \max \|H(\tilde{\eta})\|$ is an enforced capping of $\max \|H(\tilde{\eta})\|$ to enhance
 the local refinement of the solitary wave, where $p_{\text{cap}} \in (0, 1)$ is also a user-
 defined parameter.

Qualitatively, in general, the proposed UM2N method can be observed
 to move the mesh in a manner that captures the fluid dynamics of the entire
 domain, which is shown in Fig.10. Around the conical island, it can be

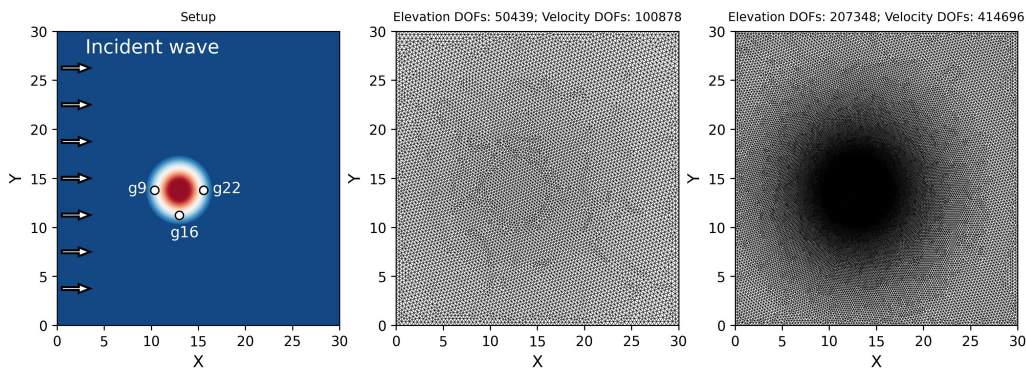


Figure 9: Conical island setup. Left: Two-dimensional plan view of bathymetry with gauges and diagram of incident wave. Middle: coarse mesh topology for numerical experiment. Right: fine mesh topology for numerical experiment.

observed that vertices are shifted to improve resolution, resolving the free-
 surface elevation as expected (See Fig. 10 and Fig. 11).

Fig. 12 shows comparisons between time series of free-surface elevations
 from mesh adaptive approaches and the fixed mesh computations. In general,
 it can be seen that the results of the non-hydrostatic model align closely with
 the available experimental data, which is consistent with the results shown
 in Pan et al. (2019). The results obtained on the three gauges show that
 UM2N movement provides results comparable in capturing the wave peak to
 those obtained on both coarse and fine mesh. These indicate that there is
 little influence of the mesh size in simulating the wave peak at these gauges.
 Despite of these results, UM2N method improve the free surface elevation in
 tracking the de-shoaling interference between the two refracted waves in the
 lee of the island (when the wave propagates around $t = 10$ s at Gauge 9),
 compared with the results on fixed coarse mesh (see Gauge 9).

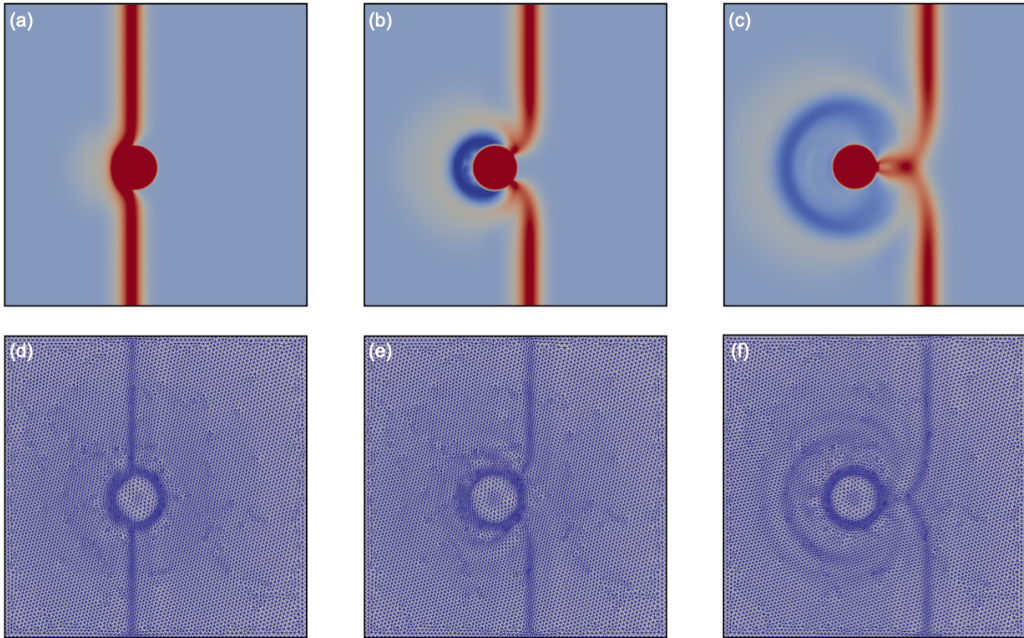


Figure 10: Conical island: Two-dimensional plan view snapshots of wave patterns (Figure **a–c**) and corresponding adapted mesh obtained via UM2N (Figure **d–f**) at different time instants, $t = 9.0, 11.0, 13.0$ s. The scale of free surface elevation range in the 2D plan view is from -0.02 to 0.04 shown by blue to red.

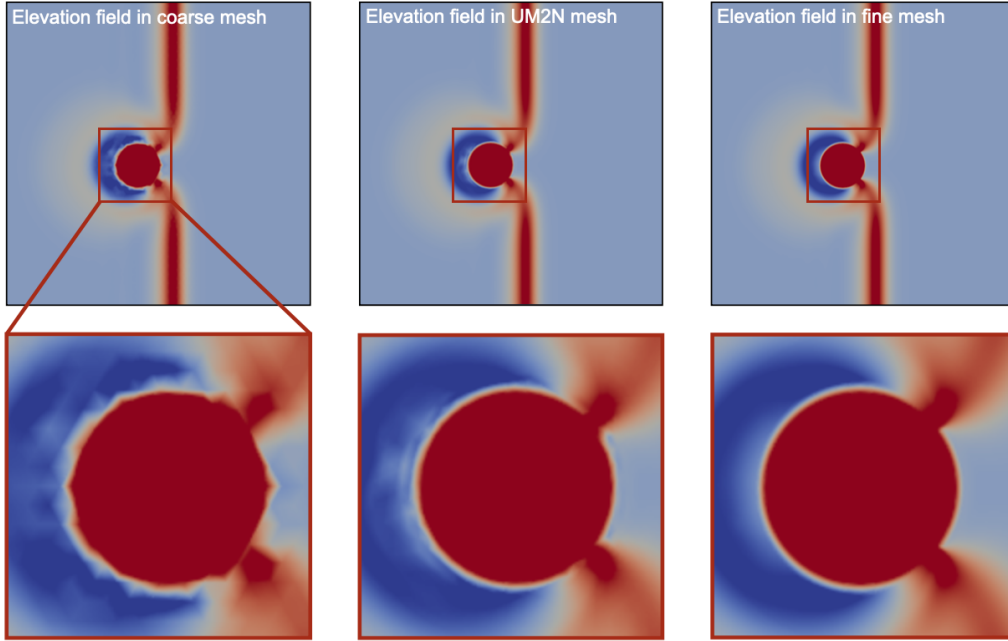


Figure 11: Conical island: Two-dimensional plan view snapshots of elevation field when the wave propagates over conical island at $t = 11.0$ s obtained via different meshes. Left: Fixed coarse mesh. Middle: UM2N adapted mesh (performed on the coarse mesh). Right: Fixed fine mesh. The scale of free surface elevation range is from -0.02 to 0.04 shown by blue to red.

Note that we intended to compare UM2N to traditional MA mesh movement for this scenario. However, MA method fails (i.e., the solver diverges) within around 100 time steps due to mesh tangling or divergence in solving the MA equation. Although insufficient numerical results are presented for this comparison, UM2N still shows its strong robustness in mesh movement.

5.4. Real-world/laboratory study case: Monai Valley

The following case study focuses on tsunami runup in Monai Valley, Japan. This is a $1/400$ scaled laboratory experiment carried at the Central Research Institute for Electric Power Industry (CRIEPI) in Abiko, Japan, which use a 205 m long, 3.4 m wide and 6 m deep tank in this laboratory experiment. In the numerical experiment, this lab benchmark case is confined to a nearshore region measuring $5.448 \text{ m} \times 3.402 \text{ m}$, as a computational

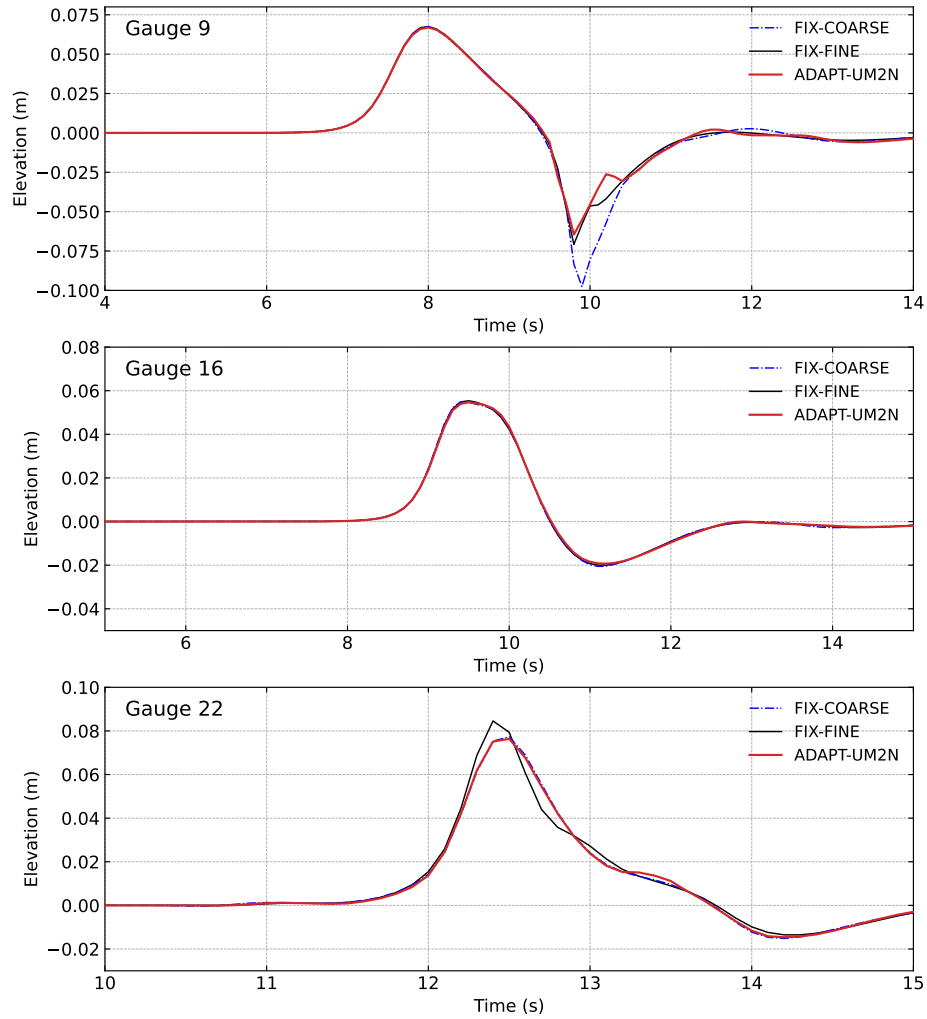


Figure 12: Comparisons of numerical results between adaptive mesh approaches and fixed mesh computations. Free-surface elevation Time series are compared among results of UM2N (red solid line), fixed coarse mesh computations (blue dashed line) and fixed fine mesh (black solid line) at three gauges for the case with $A/d = 0.181$.

domain. Initially, the tank is filled with still water, and a known incident 580
 wave moves to the shoreline from the offshore. 581

In this simulation, the coarse mesh is generated with 4,021 vertices and 582
 7,802 elements, with mesh sizes $\Delta x = 0.075$ m; the fine mesh contains 17,953 583

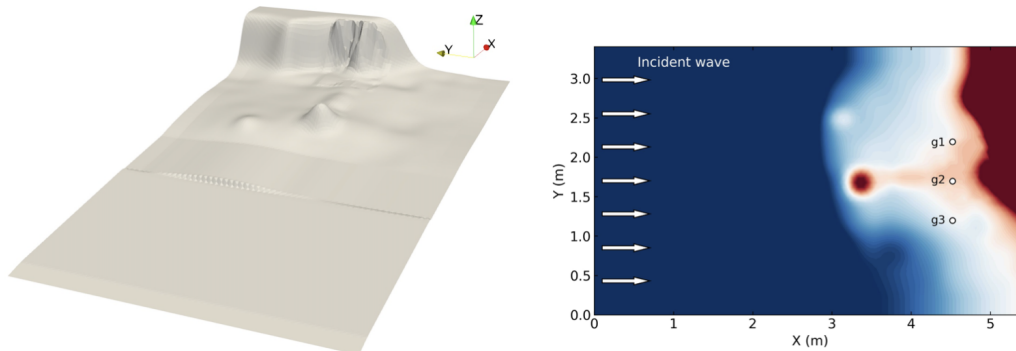


Figure 13: Monai Valley test case. Left: Bottom topography and land. Right: Setup diagram of the numerical experiment. The location (x, y) of the three gauges are $g1 = (4.521 \text{ m}, 1.196 \text{ m})$, $g2 = (4.521 \text{ m}, 1.696 \text{ m})$, and $g3 = (4.521 \text{ m}, 2.196 \text{ m})$ shown in setup diagram respectively.

vertices and 35,396 elements, with mesh sizes $\Delta x = 0.035 \text{ m}$. The bottom friction in this simulation is set as $\mu = 0.019 \text{ s} \cdot \text{m}^{-1/3}$ via 2D quadratic drag parameter in the term of bottom friction in the Eq. 17, and the magnitude of maximum horizontal velocity is set as $5.0 \text{ m} \cdot \text{s}^{-1}$. Initially, the total time duration is set as 24 s, to minimize the impact of reflection from the computational boundary, and the time step is 0.01 s. In addition, the given data of input wave is interpolated into the meshes and is updated at each timestep. The elevation data obtained in the laboratory experiment is compared with numerical results at the three locations: Gauge 1: $(x_1, y_1) = (4.521 \text{ m}, 1.196 \text{ m})$, Gauge 2: $(x_2, y_2) = (4.521 \text{ m}, 1.696 \text{ m})$, and Gauge 3: $(x_3, y_3) = (4.521 \text{ m}, 2.196 \text{ m})$, corresponding to the point $(x_0, y_0) = (0, 0)$ shown in Fig. 13.

The qualitative impact of the two mesh-adaptation strategies, UM2N and MA movement, is presented in Fig. 14. In our implementation, UM2N concentrates mesh very locally around steep free-surface gradients, producing highly refined regions near wave peaks and troughs, while relatively irregular mesh sizes and shapes away from these features. Compared with UM2N, the strategy of MA movement redistributes mesh nodes more globally, leading to smoother transitions in mesh size and improved mesh regularity and keeping enhanced resolution in the neighborhood of the wave. These observations indicate that the UM2N strategy is more aggressive in capturing wave features in a fine scale by localized adaptation, while MA movement offers a balanced

way between local refinement and overall mesh quality. (see Fig. 14). 606

In addition, Fig. 15 shows the quantitative comparisons in impact of the 607
 UM2N method for free-surface elevation time-series at three gauges. Al- 608
 though there is little influence of the mesh resolution on the given gauge 609
 locations mentioned by Ricchiuto (2015) and Arpaia and Ricchiuto (2018), 610
 the results at gauge 22 show that the UM2N and MA movement computa- 611
 tions approach closer to that of fine mesh, compared to the results of coarse 612
 mesh. Moreover, Table 1 shows the performance benchmark on Monai Val- 613
 ley test case, where UM2N achieves superior error reduction (91.14%) to the 614
 traditional MA movement (73.64%) in simulating wave peak at Gauge 3. 615

Regarding computational costs, Table 1 presents the inference time for 616
 UM2N and MA based mesh movement, where the UM2N method can be 617
 seen to significantly speed up the the inference time (~ 290 vs ~ 6 times) 618
 during the movement. 619

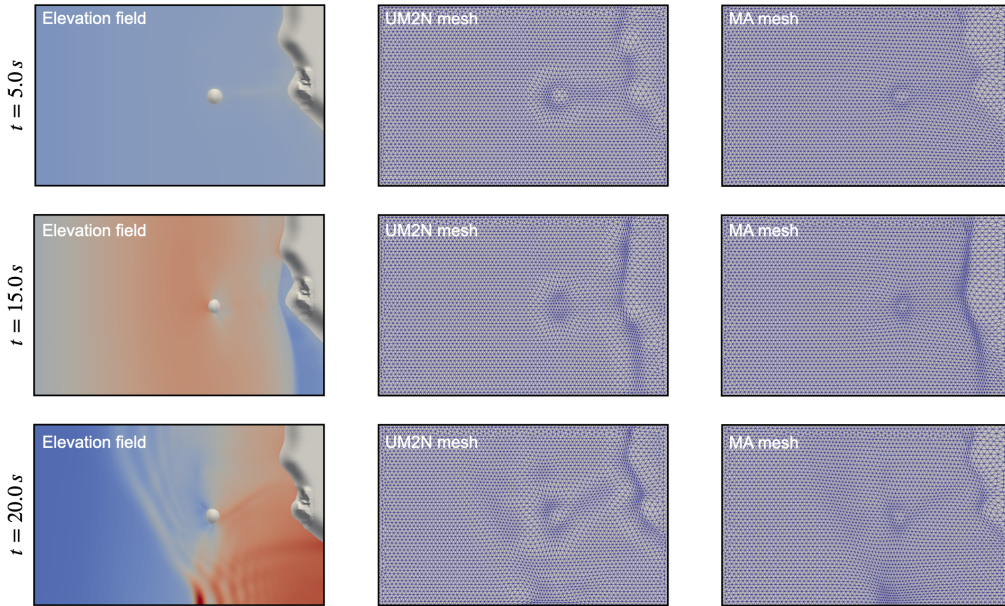


Figure 14: Monai Valley: Two-dimensional plan view snapshots of elevation field (left column) under wet-dry interface and adapted mesh using UM2N (middle column) and MA movement (right column) at different time instants, $t = 5.0, 15.0, 20.0$ s (from upper to bottom row, respectively). The scale of free surface elevation range is from -0.02 to 0.04 shown by blue to red.

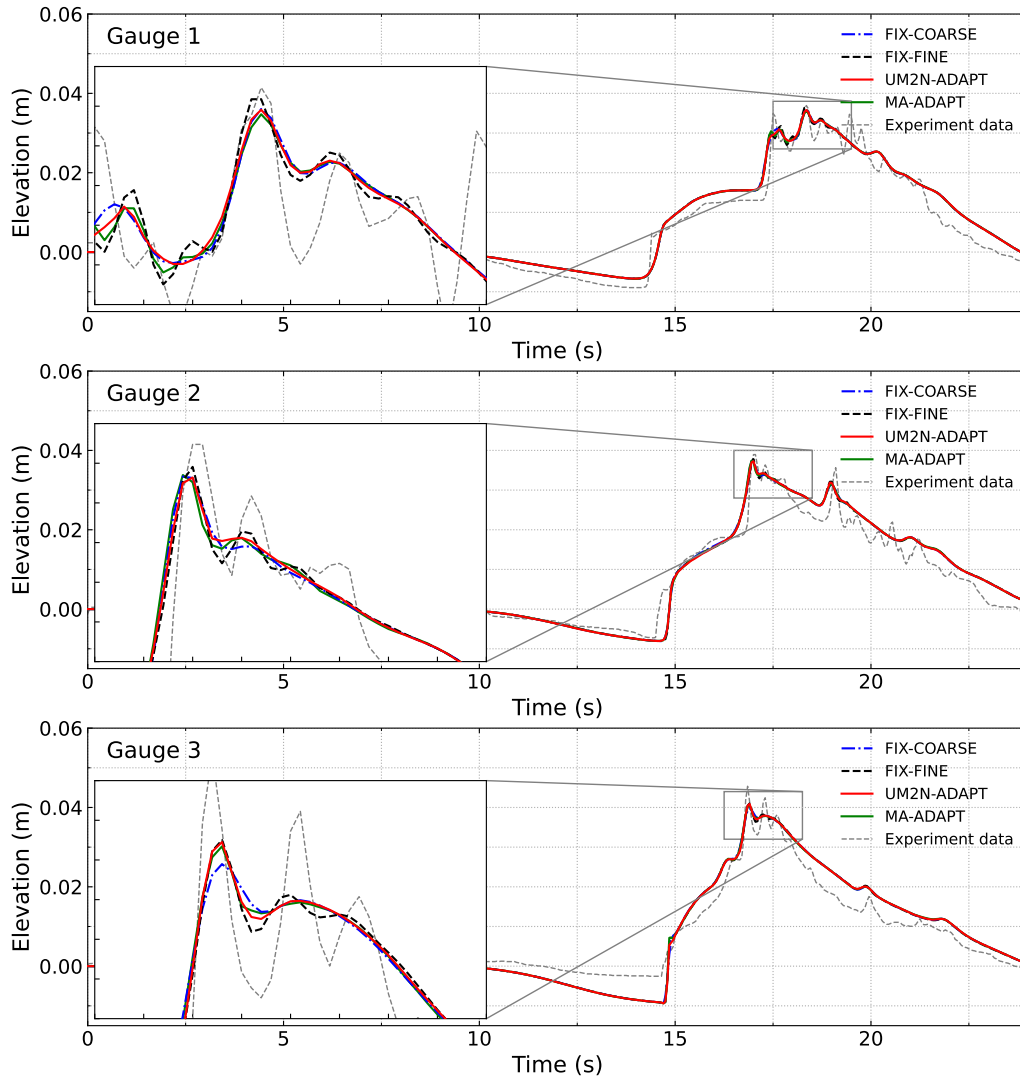


Figure 15: Comparisons of free-surface elevation time-series at three gauges in the Monai Valley test case. Free-surface elevation time series are compared among results of UM2N (red solid line), MA movement (green solid line), fixed coarse mesh (blue dashed line) and fixed fine mesh computations (black solid line).

Hardware	MA CPU	UM2N CPU	UM2N GPU (Nvidia A100)
Avg. inference time (s) ↓	12563.28	2229.08	43.34
Speedup	–	~ 6×	~ 290 ×

Table 1: Performance benchmark on Monai Valley test case. Average inference time over five runs is recorded during mesh adaptation for both UM2N and MA movement.

6. Conclusion

In this paper, the use of machine learning based mesh movement for non-hydrostatic shallow water modelling has been investigated for the simulation of complex wave interactions and tsunami run-up on irregular bathymetries and changeable boundary conditions.

Results indicate that mesh movement via the UM2N network not only offers improved accuracy but also displays more effective convergence behaviour, particularly during later stages of wave propagation, underscoring its suitability for accurately capturing complex dynamic wave phenomena using adaptive mesh refinement techniques. The solitary wave based scenarios also indicates the strong robustness of UM2N adaptation in handling the rapid changes of free surface elevation caused by water refraction. This means that UM2N is an effective surrogate model for costly MA equation-based mesh movement and that tight coupling of machine learning based mesh movement with a modern PDE framework is both feasible and practical. The approach offers an alternative way to faster, adaptive coastal modelling without losing accuracy in tsunami simulation. Moreover, new monitor functions are designed for these scenarios including a wetting-drying interface in order to track wave propagation correctly and enhance refinement in these areas.

Future research in this area will involve the extension of our framework to 3D mesh geometries, based on the work including Li et al. (2005) and Rowbottom et al. (2025). Mesh adaptive techniques based on unsupervised learning, such as G-adaptivity (Rowbottom et al., 2025), and Unsupervised and Generalizable Mesh Movement Network (UGM2N) (Wang et al., 2025) provide alternative movement strategies that could also be applied to non-hydrostatic models. Considering mesh regularity and uniformity during movement, the mesh adaptation algorithms can be further improved (e.g., allowing boundary node movement), thus helping to generate meshes with

superior quality. 649

Acknowledgements 650

YL would like to acknowledge Mingrui Zhang and Chunyang Wang for 651
their invaluable advice and technical support on the use of the UM2N model. 652
YL also gratefully thanks Wei Pan for helpful advice in benchmarking setup. 653
All authors would like to acknowledge the Imperial College London Research 654
Computing Service for their support. 655

References 656

- Arpaia, L., Ricchiuto, M., 2018. r-adaptation for Shallow Water flows: con- 657
servation, well balancedness, efficiency. *Computers & Fluids* 160, 175–203. 658
doi:10.1016/j.compfluid.2017.10.026. 659
- Balay, S., Abhyankar, S., Adams, M.F., Benson, S., Brown, J., Brune, P., 660
Buschelman, K., Constantinescu, E., Dalcin, L., Dener, A., Eijkhout, V., 661
Faibussowitsch, J., Gropp, W.D., Hapla, V., Isaac, T., Jolivet, P., Karpeev, 662
D., Kaushik, D., Knepley, M.G., Kong, F., Kruger, S., May, D.A., McInnes, 663
L.C., Mills, R.T., Mitchell, L., Munson, T., Roman, J.E., Rupp, K., Sanan, 664
P., Sarich, J., Smith, B.F., Suh, H., Zampini, S., Zhang, H., Zhang, J., 665
2025. PETSc/TAO Users Manual. Technical Report ANL-21/39 - Revision 666
3.24. Argonne National Laboratory. doi:10.2172/2998643. 667
- Brenier, Y., 1991. Polar factorization and monotone rearrangement of vector- 668
valued functions. *Communications on Pure and Applied Mathematics* 44, 669
375–417. doi:10.1002/cpa.3160440402. 670
- Briggs, M., Synolakis, C., Harkins, G., Green, D., 1995. Laboratory Ex- 671
periments of Tsunami Runup on a Circular Island. *Pure and Applied* 672
Geophysics 144, 569–593. doi:10.1007/BF00874384. 673
- Budd, C.J., Williams, J.F., 2009. Moving Mesh Generation Using the 674
Parabolic Monge–Ampère Equation. *SIAM Journal on Scientific Com-* 675
puting 31, 3438–3465. doi:10.1137/080716773. 676
- Clare, M.C.A., Wallwork, J.G., Kramer, S.C., Weller, H., Cotter, C.J., 677
Piggott, M.D., 2021. Multi-scale hydro-morphodynamic modelling using 678
mesh movement methods. *International Journal on Geomathematics* 13, 679
2. doi:10.1007/s13137-021-00191-1. 680

- Cui, H., Pietrzak, J.D., Stelling, G.S., 2012. Improved efficiency of a non-hydrostatic, unstructured grid, finite volume model. *Ocean Modelling* 54–55, 55–67. doi:10.1016/j.ocemod.2012.07.001.
- Cui, H., Pietrzak, J.D., Stelling, G.S., 2014. Optimal dispersion with minimized Poisson equations for non-hydrostatic free surface flows. *Ocean Modelling* 81, 1–12. doi:10.1016/j.ocemod.2014.06.004.
- Dalcin, L.D., Paz, R.R., Kler, P.A., Cosimo, A., 2011. Parallel distributed computing using Python. *Advances in Water Resources* 34, 1124–1139. doi:10.1016/j.advwatres.2011.04.013.
- Davis, B., LeVeque, R., 2016. Adjoint Methods for Guiding Adaptive Mesh Refinement in Tsunami Modeling. *Pure and Applied Geophysics* 173, 4055–4074. doi:10.1007/s00024-016-1412-y.
- Delzanno, G.L., Chacón, L., Finn, J.M., Chung, Y., Lapenta, G., 2008. An optimal robust equidistribution method for two-dimensional grid adaptation based on Monge–Kantorovich optimization. *Journal of Computational Physics* 227, 9841–9864. doi:10.1016/j.jcp.2008.07.020.
- Fidkowski, K.J., Chen, G., 2021. Metric-based, goal-oriented mesh adaptation using machine learning. *Journal of Computational Physics* 426, 109957. doi:10.1016/j.jcp.2020.109957.
- Ham, D.A., Kelly, P.H.J., Mitchell, L., Cotter, C.J., Kirby, R.C., Sagiya, K., Bouziani, N., Vorderwuelbecke, S., Gregory, T.J., Betteridge, J., Shapero, D.R., Nixon-Hill, R.W., Ward, C.J., Farrell, P.E., Brubeck, P.D., Marsden, I., Gibson, T.H., Homolya, M., Sun, T., McRae, A.T.T., Luporini, F., Gregory, A., Lange, M., Funke, S.W., Rathgeber, F., Bercea, G.T., Markall, G.R., 2023. *Firedrake User Manual*. Imperial College London; University of Oxford; Baylor University; University of Washington. doi:10.25561/104839.
- Hou, J., Liang, Q., Simons, F., Hinkelmann, R., 2013. A stable 2D unstructured shallow flow model for simulations of wetting and drying over rough terrains. *Computers & Fluids* 82, 132–147. doi:10.1016/j.compfluid.2013.04.015.

- Huang, K., Krügener, M., Brown, A., Menhorn, F., Bungartz, H.J., Hartmann, D., 2021. Machine Learning-Based Optimal Mesh Generation in Computational Fluid Dynamics. *arXiv:2102.12923*. 712
713
714
- Kanoğlu, U., Titov, V.V., Aydın, B., Moore, C., Stefanakis, T.S., Zhou, H., Spillane, M., Synolakis, C.E., 2013. Focusing of long waves with finite crest over constant depth. *Proceedings of the Royal Society A: Mathematical, Physical and Engineering Sciences* 469, 20130015. doi:10.1098/rspa.2013.0015. 715
716
717
718
719
- Kärnä, T., de Brie, B., Gourgue, O., Lambrechts, J., Comblen, R., Legat, V., Deleersnijder, E., 2011. A fully implicit wetting–drying method for DG-FEM shallow water models, with an application to the Scheldt Estuary. *Computer Methods in Applied Mechanics and Engineering* 200, 509–524. doi:10.1016/j.cma.2010.07.001. 720
721
722
723
724
- Kärnä, T., Kramer, S.C., Mitchell, L., Ham, D.A., Piggott, M.D., Baptista, A.M., 2018. Thetis coastal ocean model: discontinuous Galerkin discretization for the three-dimensional hydrostatic equations. *Geoscientific Model Development* 11, 4359–4382. doi:10.5194/gmd-11-4359-2018. 725
726
727
728
- Lai, Z., Chen, C., Cowles, G.W., Beardsley, R.C., 2010. A nonhydrostatic version of FVCOM: 1. Validation experiments. *Journal of Geophysical Research: Oceans* 115, C11010. doi:10.1029/2009JC005525. 729
730
731
- Li, X., Shephard, M.S., Beall, M.W., 2005. 3D anisotropic mesh adaptation by mesh modification. *Computer Methods in Applied Mechanics and Engineering* 194, 4915–4950. doi:10.1016/j.cma.2004.11.019. 732
733
734
- Liang, D., Liu, H., Tang, H., Rana, R., 2013. Comparison Between Boussinesq and Shallow-Water Models in Predicting Solitary Wave Runup on Plane Beaches. *Coastal Engineering Journal* 55, 1350014–1–1350014–24. doi:10.1142/S0578563413500149. 735
736
737
738
- Lynett, P.J., Wu, T.R., Liu, P.L.F., 2002. Modeling wave runup with depth-integrated equations. *Coastal Engineering* 46, 89–107. doi:10.1016/S0378-3839(02)00043-1. 739
740
741
- Ma, G., Shi, F., Kirby, J.T., 2012. Shock-capturing non-hydrostatic model for fully dispersive surface wave processes. *Ocean Modelling* 43–44, 22–35. doi:10.1016/j.ocemod.2011.12.002. 742
743
744

- Marshall, J., Hill, C., Perelman, L., Adcroft, A., 1997. Hydrostatic, quasi-hydrostatic, and nonhydrostatic ocean modeling. *Journal of Geophysical Research: Oceans* 102, 5733–5752. doi:10.1029/96JC02776.
- McRae, A.T.T., Cotter, C.J., Budd, C.J., 2018. Optimal-Transport-Based Mesh Adaptivity on the Plane and Sphere Using Finite Elements. *SIAM Journal on Scientific Computing* 40, A1121–A1148. doi:10.1137/16M1109515.
- Nikolos, I.K., Delis, A.I., 2009. An unstructured node-centered finite volume scheme for shallow water flows with wet/dry fronts over complex topography. *Computer Methods in Applied Mechanics and Engineering* 198, 3723–3750. doi:10.1016/j.cma.2009.08.006.
- Pan, W., Kramer, S.C., Piggott, M.D., 2019. Multi-layer non-hydrostatic free surface modelling using the discontinuous galerkin method. *Ocean Modelling* 134, 68–83. doi:10.1016/j.ocemod.2019.01.003.
- Pan, W., Kramer, S.C., Piggott, M.D., 2021. A σ -coordinate non-hydrostatic discontinuous finite element coastal ocean model. *Ocean Modelling* 157, 101732. doi:10.1016/j.ocemod.2020.101732.
- Piggott, M.D., Pain, C.C., Gorman, G.J., Power, P.W., Goddard, A.J.H., 2005. h, r, and hr adaptivity with applications in numerical ocean modelling. *Ocean Modelling* 10, 95–113. doi:10.1016/j.ocemod.2004.07.007.
- Ricchiuto, M., 2015. An explicit residual based approach for shallow water flows. *Journal of Computational Physics* 280, 306–344. doi:10.1016/j.jcp.2014.09.027.
- Rowbottom, J., Maierhofer, G., Deveney, T., Mueller, E., Paganini, A., Schratz, K., Liò, P., Schönlieb, C.B., Budd, C., 2025. G-Adaptivity: optimised graph-based mesh relocation for finite element methods. [arXiv:2407.04516](https://arxiv.org/abs/2407.04516).
- Shi, F., Tehranirad, B., Kirby, J.T., Harris, J.C., Grilli, S., 2013. FUNWAVE-TVD: Fully Nonlinear Boussinesq Wave Model with TVD Solver, Documentation and User’s Manual (Version 2.1). Technical Report CACR-11-04. Center for Applied Coastal Research, University of Delaware. Newark, Delaware.

- Song, W., Zhang, M., Wallwork, J.G., Gao, J., Tian, Z., Sun, F., Piggott, M.D., Chen, J., Shi, Z., Chen, X., Wang, J., 2024. M2N: mesh movement networks for pde solvers, in: Proceedings of the 36th International Conference on Neural Information Processing Systems, Curran Associates, Inc. 777
778
779
780
781
- Stansby, P.K., Zhou, J.G., 1998. Shallow-water flow solver with non-hydrostatic pressure: 2D vertical plane problems. International Journal for Numerical Methods in Fluids 28, 541–563. doi:10.1002/(SICI)1097-0363(19980915)28:3<541::AID-FLD738>3.0.CO;2-0. 782
783
784
785
- Stelling, G., Zijlema, M., 2003. An accurate and efficient finite-difference algorithm for non-hydrostatic free-surface flow with application to wave propagation. International Journal for Numerical Methods in Fluids 43, 1–23. doi:10.1002/flid.595. 786
787
788
789
- Tadepalli, S., Synolakis, C.E., 1994. The run-up of N-waves on sloping beaches. Proceedings of the Royal Society of London A: Mathematical and Physical Sciences 445, 99–112. 790
791
792
- Wallwork, J.G., 2021. Mesh adaptation and adjoint methods for finite element coastal ocean modelling. Ph.D. thesis. Imperial College London. doi:10.25560/92820. 793
794
795
- Wang, Z., Chen, X., Wang, Q., Gao, X., Zhang, Q., Jia, M., Zhang, X., Liu, J., 2025. UGM2N: An Unsupervised and Generalizable Mesh Movement Network via M-Uniform Loss. arXiv:2508.08615. 796
797
798
- Wei, G., Kirby, J.T., 1995. Time-Dependent Numerical Code for Extended Boussinesq Equations. Journal of Waterway, Port, Coastal, and Ocean Engineering 121, 251–261. doi:10.1061/(ASCE)0733-950X(1995)121:5(251). 799
800
801
802
- Wei, Z., Jia, Y., 2013. A depth-integrated non-hydrostatic finite element model for wave propagation. International Journal for Numerical Methods in Fluids 73, 976–1000. doi:10.1002/flid.3832. 803
804
805
- Yang, J., Dzanic, T., Petersen, B., Kudo, J., Mittal, K., Tomov, V., Camier, J.S., Zhao, T., Zha, H., Kolev, T., Anderson, R., Faissol, D., 2023. Reinforcement Learning for Adaptive Mesh Refinement. arXiv:2103.01342. 806
807
808

- Zhang, M., Wang, C., Kramer, S., Wallwork, J.G., Li, S., Liu, J., Chen, X., Piggott, M.D., 2024. Towards Universal Mesh Movement Networks. *Advances in Neural Information Processing Systems* 36. doi:10.1007/978-3-030-50420-5_14.
- Zhang, Z., Wang, Y., Jimack, P.K., Wang, H., 2020. MeshingNet: A New Mesh Generation Method Based on Deep Learning, in: *Computational Science – ICCS 2020: 20th International Conference, Amsterdam, The Netherlands, June 3–5, 2020, Proceedings, Part III*, Springer-Verlag. pp. 186–198. doi:10.1007/978-3-030-50420-5_14.
- Zijlema, M., Stelling, G., Smit, P., 2011. SWASH: An operational public domain code for simulating wave fields and rapidly varied flows in coastal waters. *Coastal Engineering* 58, 992–1012. doi:10.1016/j.coastaleng.2011.05.015.
- Zijlema, M., Stelling, G.S., 2005. Further experiences with computing non-hydrostatic free-surface flows involving water waves. *International Journal for Numerical Methods in Fluids* 48, 169–197.